Nano Research 2018, 11(9): 4562–4573
https://doi.org/10.1007/s12274-018-2036-6
Research Article
ISSN 1998-0124
CN 11-5974/O4

Dual confinement of polysulfides in boron-doped porous carbon sphere/graphene hybrid for advanced Li-S batteries

Wei Ai[1,2,§], Jiewei Li[1,§], Zhuzhu Du[1], Chenji Zou[2], Hongfang Du[2,4], Xin Xu[2], Yu Chen[2], Hongbo Zhang[2], Jianfeng Zhao[1], Changming Li[4], Wei Huang[1,3] (✉), and Ting Yu[2] (✉)

[1] *Key Laboratory of Flexible Electronics (KLOFE) & Institute of Advanced Materials (IAM), Jiangsu National Synergetic Innovation Center for Advanced Materials (SICAM), Nanjing Tech University (NanjingTech), 30 South Puzhu Road, Nanjing 211816, China*
[2] *Division of Physics and Applied Physics, School of Physical and Mathematical Sciences, Nanyang Technological University, 50 Nanyang Avenue, Singapore 637371, Singapore*
[3] *Shaanxi Institute of Flexible Electronics (SIFE), Northwestern Polytechnical University (NPU), 127 West Youyi Road, Xi'an 710072, China*
[4] *Institute for Clean Energy & Advanced Materials, Southwest University, Chongqing 400715, China*
[§] *Wei Ai and Jiewei Li contributed equally to this work.*

Received: 13 September 2017
Revised: 1 February 2018
Accepted: 11 February 2018

© Tsinghua University Press and Springer-Verlag GmbH Germany, part of Springer Nature 2018

KEYWORDS
potato starch
carbon spheres
graphene
boron doping
Li-S batteries

ABSTRACT

A hybrid structure consisting of boron-doped porous carbon spheres and graphene (BPCS-G) has been designed and synthesized toward solving the polysulfide-shuttle problem, which is the most critical issue of current Li-S batteries. The proposed hybrid structure showing high surface area (870 $m^2 \cdot g^{-1}$) and high B-dopant content (6.51 wt.%) simultaneously offers both physical confinement and chemical absorption of polysulfides. On one hand, the abundant-pore structure ensures high sulfur loading, facilitates fast charge transfer, and restrains polysulfide migration during cycling. On the other hand, our density functional theory calculations demonstrate that the B dopant is capable of chemically binding polysulfides. As a consequence of such dual polysulfide confinement, the BPCS-G/S cathode prepared with 70 wt.% sulfur loading presents a high reversible capacity of 1,174 $mAh \cdot g^{-1}$ at 0.02 C, a high rate capacity of 396 $mAh \cdot g^{-1}$ at 5 C, and good cyclability over 500 cycles with only 0.05% capacity decay per cycle. The present work provides an efficient and cost-effective platform for the scalable synthesis of high-performance carbon-based materials for advanced Li-S batteries.

1 Introduction

Owing to the reversible multielectron transfer chemical reaction between lithium and sulfur, lithium-sulfur (Li-S) batteries are, in principle, capable of affording high energy densities up to 2,600 $Wh \cdot kg^{-1}$, over six-fold

Address correspondence to Ting Yu, yuting@ntu.edu.sg; Wei Huang, iamwhuang@njtech.edu.cn

higher than those of conventional lithium-ion batteries [1–3]. However, they have yet to be commercialized owing to unsettled issues including (1) the insulation of sulfur and its discharge product, Li_2S; (2) the large volumetric variation (over 80%) between sulfur and Li_2S; and (3) the dissolution and migration of intermediate polysulfides (Li_2S_n, $n \geq 4$) in the electrolyte [4–6]; all of which lead to poor electrochemical performances of batteries, for example, low specific capacities, low Coulombic efficiencies, and short cycle lives [7]. To this end, an appropriate conductive matrix is generally required in order to ensure efficient sulfur cathode utilization and fast electron transport, cushion volume expansion, and simultaneously trap soluble polysulfides.

Carbon-based materials are ideal hosts for sulfur owing to their availabilities and remarkable physicochemical properties (i.e., low densities, good chemical stabilities, and high electronic conductivities), environmental friendliness, and low cost [8–10]. Since the pioneering work of studying the encapsulation of sulfur in porous carbon by Wang et al. [11, 12], numerous similar carbon/sulfur composites subsequently have been reported using micro-, meso-, macro-, and hierarchical porous carbons including carbon spheres, carbon black, carbon nanotubes, graphene, carbon nanofibers, and their hybrids [2, 13–15]. Despite the achievements of significantly improved electrochemical performances of such composites, their long-term cyclabilities are still dissatisfactory because physical confinement by means of structural design, i.e., morphological engineering and pore structure regulation, is insufficient to suppress the polysulfide shuttle. Furthermore, the weak interfacial interactions between nonpolar carbon surfaces and polar polysulfides are kinetically unfavorable for limiting polysulfide migration.

In response to these problems, functionalized carbon-based hosts, for example, heteroatom-doped carbons (i.e., carbons doped with B, N, P, S, and halogen atoms) showing stronger affinities for polysulfides have been developed [16–18]. Boron is different from its dopant counterparts because it is an electron-deficient atom that shows lower electronegativity with respect to carbon, so B doping can cause σ electrons locate on carbon atoms thereby decreasing the electron densities of delocalized π electrons on carbon atoms as well as reducing the total electron density [19]. All such changes would lead to a positively polarized carbon surface that is beneficial for the chemisorption of negatively charged polysulfides. As a consequence, B-doped carbon/S composites have shown superior electrochemical performances, such as higher specific capacities, longer cyclic stabilities, and better rate capabilities, than nondoped carbon/S and N-doped carbon/S composites [20, 21]. However, the low surface areas of B-doped carbons result in inadequate contact areas for sulfur impregnation, leading to hybrid materials showing active mass loadings below 60 wt.%, substantially offseting the fascinating energy storage capabilities of Li-S batteries. B-doped carbons, on the other hand, are fabricated by post-annealing, meaning that the carbon matrices are directly subjected to high temperatures in the presence of boron sources (i.e., H_3BO_3 and B_2O_3) [22–24], which intrinsically brings about low B contents (< 3 wt.%) compared with *in situ* pyrolysis [25–27], thereby lacking efficacious polysulfide binding. Therefore, the exploration of an effective scheme for constructing high-surface-area B-doped carbon-based hosts, especially highly B doped ones, for advanced Li-S batteries is crucial but remains challenging.

In this work, we demonstrate an efficient and cost-effective strategy for the scalable synthesis of highly B-doped carbon via *in situ* carbonization of B-containing polysaccharide. We show that hybrid host materials based on boron-doped porous carbon spheres (BPCSs) and graphene can show combined physical and chemical sulfur confinement. In this well-designed architecture, the pore structures serve as vessels to encapsulate and immobilize the active material via physisorption, whereas the B dopant is capable of binding polysulfides through strong chemisorption. Such dual confinement action can effectively suppress polysulfide shuttling during discharging and charging, thus conferring outstanding electrochemical performances for Li-S batteries, including high reversible capacity (1,174 $mAh \cdot g^{-1}$), excellent cycling stability (500 cycles with a low capacity decay of 0.05% per cycle), and good rate performance (396 $mAh \cdot g^{-1}$ at 5 C).

2 Experimental

2.1 Preparation of carbon hosts

7.41 g of boric acid was first dissolved in 180 mL of deionized water, and 3.0 g of potato starch (PS) was then added to the solution. The suspension was vigorously stirred for 20 min and was then transferred into a 200-mL ZX-TFM autoclave, which was sealed and heated at 200 ℃ for 24 h. The black-brown precipitate was collected by filtration, washed with deionized water, and dried at 100 ℃ overnight.

2.2 Preparation of BPCSs

2 g of the product was dispersed in 34 mL of KOH solution (3.2 M) under constant stirring. Subsequently, the solution was evaporated on a hotplate, and the clod-like sample was calcined in a tube furnace. The furnace was heated to pyrolysis temperature (700, 800, or 900 ℃) for 2 h, ramped 5 ℃·min^{-1} in Ar, and the as-obtained products were denoted as BPCS-700, BPCS-800, or BPCS-900, respectively. The resulting BPCSs were treated with 300 mL of HCl (6 M) overnight, then filtrated and washed repeatedly with deionized water until the pH of the solutions reached 7. The samples were finally dried at 100 ℃ in a drying oven.

2.3 Preparation of BPCS-800/graphene hybrid (BPCS-800-G)

For the synthesis of BPCS-800-G, additional graphene oxide (GO) dispersion (100 mL, 5 mg·mL^{-1}) was added dropwise to the KOH-containing polymer precursor solution, while the other experimental parameters were not changed.

2.4 Preparation of PS-derived carbon (PSC)

Since starch can be easily hydrolyzed into glucose and fructose when mixed with KOH, PSC was synthesized by directly annealing PS at 800 ℃ in a tube furnace.

2.5 Preparation of BPCS-800/S, BPCS-800-G/S, and PSC/S composites

0.6 g of a carbon host; that is, BPCS-800, BPCS-800-G, or PSC, was mixed with 1.4 g of sulfur and was adequately ground in a mortar. The mixture was then transferred into a 20-mL sealed stainless steel autoclave and was maintained at 160 ℃ for 12 h.

2.6 Characterizations

Scanning electron microscopy (SEM) and elemental mapping images of the samples were recorded on a Zeiss Auriga Dual-Beam FIB/SEM instrument coupled with energy-dispersive X-ray spectroscopy (EDS). The textural properties were examined by a Micromeritics ASAP 2020 instrument at 77 K. The Brunauer–Emmett–Teller (BET) surface areas were obtained by N_2 adsorption and desorption isotherms, whereas the pore size distributions were analyzed using density functional theory (DFT). X-ray diffraction (XRD) patterns were measured on a D8 ADVANCE diffractometer (40 kV, 30 mA, Bruker) equipped with Cu Kα (λ = 1.5418 Å) radiation. Electrical conductivity measurements were performed on a Keithley 4200 semiconductor characterization system using a 4-point probe method. Raman spectra were acquired on a WITEC CRM200 Raman system with a 532-nm laser source. Thermogravimetric analysis (TGA) was carried out on a TGA Q500 apparatus ramped at 10 ℃·min^{-1} in N_2. Elemental analysis was recorded on a FLASH 2000 organic elemental analyzer. X-ray photoelectron spectroscopy (XPS) measurements were conducted on a VG ESCALAB MK II instrument with Al Kα (1,486.6 eV) radiation. Material compaction densities were obtained using a hydraulic press machine under 10 tons of pressure to guarantee high densities and mechanical strengths. The compaction densities were calculated based on the formula $\rho = m/(d \times \pi \times r^2)$, where r is the radius, m is the mass, and d is the thickness of the corresponding cakes.

2.7 Theoretical calculations

The pristine-carbon model was constructed using 75 carbon atoms terminated by hydrogen atoms at the edges. To simulate oxygen functional groups in carbon, we also built one model each in which carbonyl and or hydroxyl groups were bonded to the carbon edges. For modeling B-doped carbon, two B atoms were incorporated into the carbon lattice. The B3LYP method with Grimme dispersion correction was used for all the calculations at the 6-311G (d, p) level in Gaussian 09 software [28]. All the constructed structures were

fully optimized, and the corresponding interaction energy (IE) and charge density difference (CDD) were calculated based on the optimized geometries. IE was defined as follows: $E_{IE} = E_{total} - E_{(C)} - E_{(S)}$, where E_{total} is the total energy of the optimized pristine carbon or B-doped carbon absorbed with S_8, Li_2S, or Li_2S_4. $E_{(C)}$ and $E_{(S)}$ are the energies of the isolated pristine or B-doped carbon and S_8, Li_2S, or Li_2S_4, respectively, where the geometry was frozen in the optimized complexes. Larger negative IE values are indicative of more thermodynamically stable complexes and, consequently, greater polysulfide binding abilities.

2.8 Electrochemical characterizations

All the batteries (CR2032 coin cells) were assembled in an Ar-filled UNIlab Pro glovebox workstation (H_2O < 0.1 ppm, O_2 < 0.1 ppm) with Li foil as the counter electrode. The electrolyte was 1 mol·L^{-1} lithium bis(trifluoromethanesulphonyl)imide dissolved in 1,3-dioxolane/1,2-dimethoxyethane (1:1 v/v) mixed with 0.2 mol·L^{-1} $LiNO_3$ to passivate the Li anode surface. The working electrodes were prepared by mixing 70 wt.% active material with 20 wt.% carbon black and 10 wt.% polyvinylidene difluoride binder in N-methyl-2-pyrrolidone to form homogeneous slurry, which was then evenly cast onto a clean aluminum foil and dried at 60 ℃ in a vacuum oven. The mass of sulfur loaded on each 12-mm-diameter round punched current collector was determined as 1.0–1.3 mg·cm^{-2} using a Semi-Micro balance (0.01 mg accuracy). For each battery, 50 μL of electrolyte were used. Cyclic voltammograms (CVs), electrochemical impedance spectroscopy (EIS) and galvanostatic charge–discharge measurements of the batteries were recorded on a CHI 760D electrochemical workstation and a Neware battery tester, respectively. All the cell electrochemical behaviors were measured in a cutoff window in the range 1.8–2.8 V. The CVs were swept at 0.5 mV·s^{-1}. The batteries were aged for 4 h to reach equilibrium before the electrochemical tests were conducted.

3 Results and discussion

The syntheses of the BPCSs prepared using PS and boric acid as the precursors are illustrated in Fig. 1(a). PS was purchased from the supermarket in Singapore (NTUC FairPrice), and the price of 350 g was only $1.50 (Fig. S1 in the Electronic Supplementary Material (ESM)). Under hydrothermal conditions, the hydroxyl groups in the PS reacted with the boric acid to form black-brown boronated PS [29], as shown in Fig. S2 in the ESM. After subsequent carbonization, the boronated-PS precursor was converted into the BPCS materials by annealing at 700, 800, or 900 ℃ to optimize the surface areas, pore structures, and B contents of the BPCSs. SEM images (Figs. 1(b)–1(d)) reveal that the samples were composed of aggregated clusters of spheres showing no obvious morphological differences. The corresponding EDS mapping images (Fig. S3 in the ESM) suggest the incorporation of B into the carbon matrices. XPS measurements were performed to probe the chemical states of the B atoms (Figs. 2(a) and 2(b)). The B contents were measured as 3.31 at.%, 1.90 at.%, and 1.12 at.% for BPCS-700, BPCS-800, and BPCS-900, respectively. High-resolution B 1s XPS spectra of the BPCS materials (Fig. 2(b)) showed two deconvoluted peaks at about 190.1 and 192.6 eV, which could be ascribed to BC_2O and BCO_2, respectively [20, 30]. More detailed elemental compositions of the BPCS

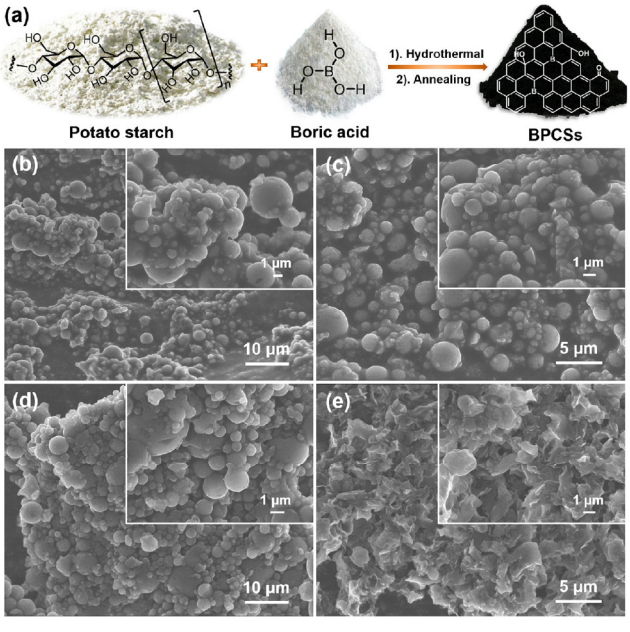

Figure 1 (a) Synthesis of BPCS materials. Background images are corresponding sample photographs. SEM images of (b) BPCS-700, (c) BPCS-800, (d) BPCS-900, and (e) BPCS-800-G. Insets are higher-magnification SEM images of corresponding samples.

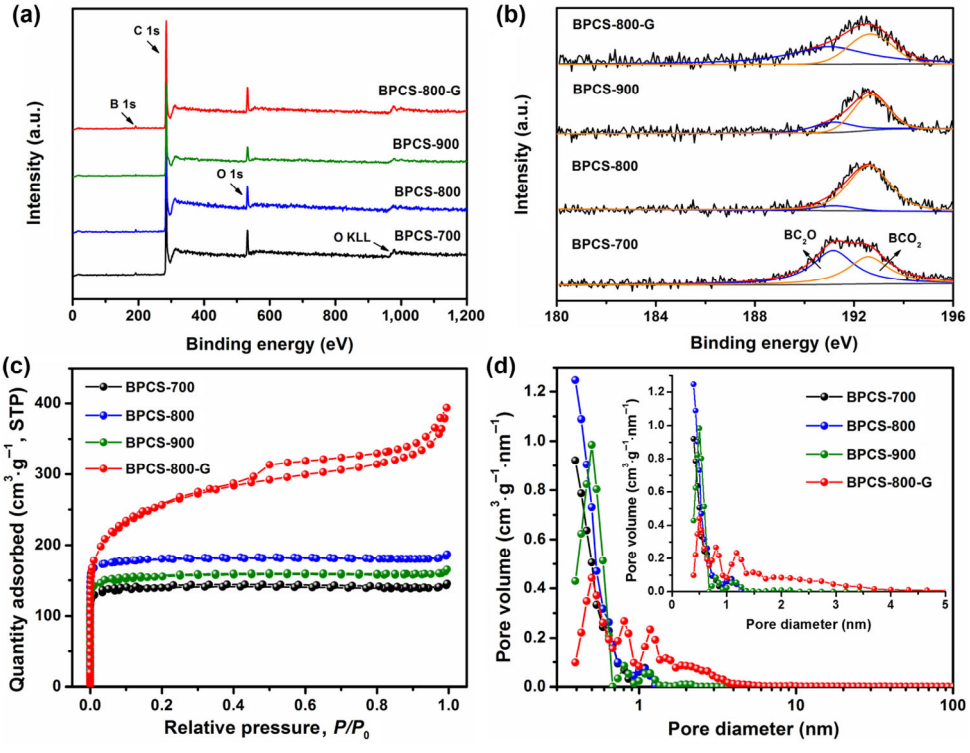

Figure 2 (a) XPS survey spectra, (b) high-resolution B 1s XPS spectra, and (c) N_2 sorption isotherms of BPCS-700, BPCS-800, BPCS-900, and BPCS-800-G. (d) Pore size distribution curves of corresponding samples obtained using DFT. Inset shows magnified 0–5-nm region.

bulk materials were obtained by elemental analysis (Table S1 in the ESM). The B contents were calculated as 12.70 wt.%, 6.74 wt.%, and 3.85 wt.% in BPCS-700, BPCS-800, and BPCS-900, respectively. In XRD patterns (Fig. S4 in the ESM), all the samples exhibited two diffraction peaks. The broad hump-shaped one centered at $2\theta \approx 19°$ suggested the samples contained amorphous carbon, while the other one at $2\theta \approx 43°$ was assigned to the (100) plane of carbon [27, 31, 32]. The N_2 isothermal adsorption and desorption (Fig. 2(c)) of the BPCS-800-G sample and the BPCS-700, BPCS-800, and BPCS-900 samples showed almost type IV and type I patterns, respectively, and steep initial uptakes ($P/P_0 < 0.01$) owing to their porous structures [33, 34]. The pore size distribution curves (Fig. 2(d)) suggested that the samples showed narrow pore distributions, mainly in the micropore range. The pore structure parameters including BET surface area, average pore diameter, and total pore volume are summarized in Table S1 in the ESM for comparison. Clearly, BPCS-800 shows a BET surface area of 539 $m^2 \cdot g^{-1}$ and a total pore volume of 0.28 $cm^3 \cdot g^{-1}$, larger than those of BPCS-700 (458 $m^2 \cdot g^{-1}$, 0.22 $cm^3 \cdot g^{-1}$) and BPCS-900 (520 $m^2 \cdot g^{-1}$, 0.26 $cm^3 \cdot g^{-1}$). Therefore, 800 °C was the optimial temperature that endowed BPCSs with superior structures such as incomplete graphitization, appropriate dopant concentration, high specific surface area, and large pore volume, all of which are vitally important characteristics of host materials for sulfur cathodes.

To further improve the physicochemical properties of the BPCSs, graphene was introduced by pyrolyzing the boronated-PS/GO mixture at 800 °C (see Experimental Section for details). Figure 1(e) shows the SEM image of the resultant BPCS-800-G hybrid, which displays an interconnected porous structure containing BPCSs encapsulated in or attached to the graphene sheets. The B content of BPCS-800-G was 1.94 at.% and 6.51 wt.% based on XPS and elemental analysis (Figs. 2(a) and 2(b) and Table S1 in the ESM), respectively, comparable to that of BPCS-800. Further, compared with the XRD pattern of BPCS-800, that of BPCS-800-G (Fig. S4 in the ESM) exhibited a newly emerged diffraction peak at $2\theta \approx 24.6°$, which was assigned to the restacked graphene layers in the

hybrid texture [35, 36]. After the introduction of graphene, the electronic conductivity of BPCS-800-G (0.56 $S \cdot cm^{-1}$) was approximately 20 times higher than that of BPCS-800 (0.029 $S \cdot cm^{-1}$), which will guarantee fast and efficient electron transport during electrochemical reactions. Moreover, the BPCS-800-G hybrid also showed a substantially increased BET surface area of 870 $m^2 \cdot g^{-1}$ and a total pore volume of up to 0.61 $cm^3 \cdot g^{-1}$ (Figs. 2(c) and 2(d) and Table S1 in the ESM), implying that BPCS-800 can integrate well with graphene to create a hierarchical pore architecture. Such an attractive porous structure is not only favorable for accommodating high-mass sulfur loading but also helpful for high active material utilization and for buffering the associated changes in volume [37]. Importantly, the rich porosity will behave like a reservoir for physically restricting soluble polysulfides in the cathodic region for high-energy-density Li-S batteries.

The BPCS-800-G/S composite was fabricated following conventional melt diffusion [38]. The corresponding SEM images are shown in Figs. 3(a) and 3(b), illustrating that sulfur had infiltrated into the porous structure or had adsorbed onto the surface or into the macropores of the BPCS-800-G hybrid. The EDS layered image (Fig. 3(c)) and elemental mapping images (Figs. 3(d)–3(g)) suggest that the sulfur distribution was in good agreement with the shape of the randomly selected area. For comparison, the BPCS-800/S composite was prepared with the same sulfur loading content as the BPCS-800-G/S composite, and the corresponding SEM images (Fig. S5 in the ESM) did not show any significant structural changes compared to the BPCS-800 SEM images. XRD patterns (Fig. 4(a)) indicated that both composites contained crystalline sulfur (JCPDS no. 08-0247) [39, 40], consistent with the Raman spectra (Fig. 4(b)). The sulfur loading ratios of the BPCS-800/S and BPCS-800-G/S composites were determined as 70 wt.% according to the TGA curves (Fig. 4(c)), which was further confirmed by weighing the samples before and after annealing (Fig. S6 in the ESM). The slight weight losses were acceptable and within the experimental error. Additionally, it is interesting to note that the TGA curves displayed two sections of weight loss. The rapid one from 160 to 240 ℃ could be assigned to the evaporation of surface-absorbed sulfur, whereas the slow one from 240 to 400 ℃ was ascribed to the removal of pore-confined sulfur [34].

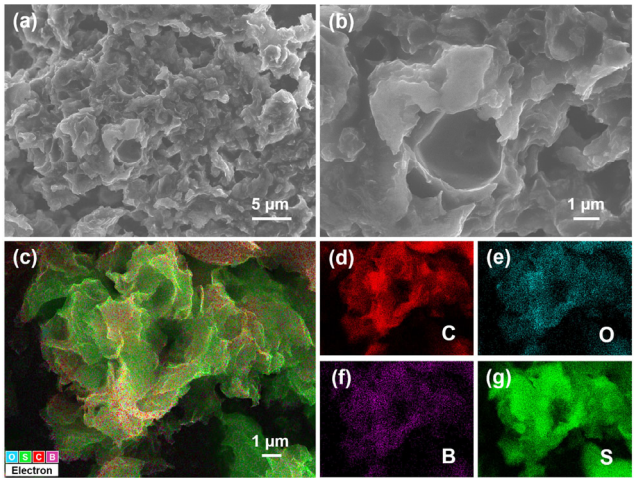

Figure 3 (a) and (b) SEM images of BPCS-800-G/S composite at different magnifications. (c) EDS layered image of BPCS-800-G/S composite and corresponding elemental mapping images of (d) C, (e) O, (f) B, and (g) S.

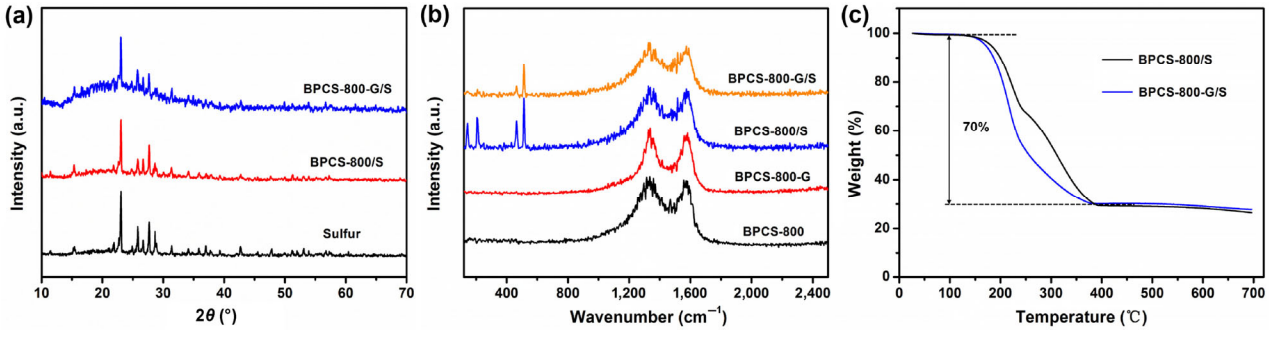

Figure 4 (a) XRD patterns of BPCS-800/S and BPCS-800-G/S composites, and of sulfur powder. (b) Raman spectra of BPCS-800, BPCS-800-G, BPCS-800/S, and BPCS-800-G/S composites. (c) TGA curves of BPCS-800/S and BPCS-800-G/S composites recorded in N_2 between room temperature and 700 °C.

To specifically determine the influence of B content on sulfur-containing molecule binding, theoretical calculations were conducted using DFT. Here, we used S_8 (starting material), Li_2S (discharge product), and Li_2S_4 (intermediate product) models to probe the interactions between B-doped carbon and sulfur species. The fully optimized configurations of S_8, Li_2S, and Li_2S_4 adsorbed on pristine-carbon surfaces are shown in Figs. 5(a)–5(c) (top view) and Figs. 5(d)–5(f) (side view), respectively. The corresponding IEs of each adsorption pair are summarized in Table 1, where larger negative E_{IE} values indicate more thermodynamically stable final products and hence higher binding energies. From the results, although pristine carbon clearly was favorable for absorbing sulfur to form a compatible structure, its affinities for adsorbing Li_2S and Li_2S_4 were relatively weak, corresponding to physical absorptions showing IEs of −0.67 and −0.82 eV, respectively, which were further confirmed by CDD images (Figs. 5(g)–5(i)) showing subtle rearrangements of electrons in sulfur-absorbed carbon and negligible perturbations in Li_2S- and Li_2S_4-absorbed carbon, respectively. Therefore, polysulfides would dissolve into the electrolyte during discharging and charging instead of adsorbing onto the carbon srfaces leading to ceaseless capacity fading in Li-S batteries, which agrees well with the previously reported experimental results [41, 42]. By sharp contrast, B-doped carbon revealed larger IEs with the sulfur species (e.g., −1.18, −2.79, and −1.15 eV for S_8, Li_2S, and Li_2S_4, respectively, Figs. 5(j)–5(o) and Table 1) than pristine carbon, signifying B doping can induce chemical absorption and potent affinity with both electron-abundant sulfur and polar sulfur-based anions. Furthermore, the obvious CDD map deformations (Figs. 5(p)–5(r)) once again document the much stronger chemical interactions between the B-doped carbon framework and sulfur species. Such powerful bonding forces would effectively restrain polysulfide shuttling, resulting in long-term cyclability. Overall, our theoretical results exclusively verified that doping carbon with B could induce additional chemical bonding of polarized sulfur discharge products, which is believed to deliver better performance than pure carbon. To further verify

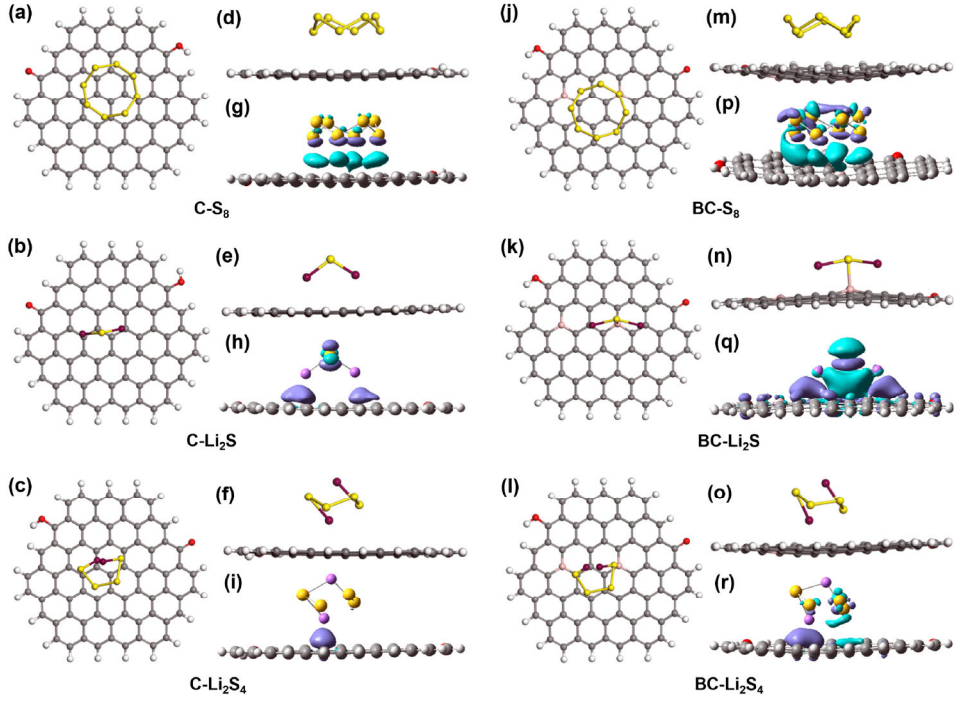

Figure 5 Optimized geometric configurations of S_8, Li_2S, and Li_2S_4 absorbed on pristine carbon and B-doped carbon surfaces. (a)–(c) and (j)–(l) Top view. (d)–(f) and (m)–(o) Side view. White, grey, red, pink, yellow, and purple spheres represent H, C, O, B, S, and Li atoms, respectively. (g)–(i) and (p)–(r) Corresponding CDD images of each adsorption pair. Cambridge blue and turquoise regions indicate increased and decreased charge densities, respectively. The isovalue is 0.0015.

Table 1 Summary of IEs for different sulfur species absorbed on pristine and B-doped carbon surfaces

Sample	S_8	Li_2S	Li_2S_4
Pristine carbon	–1.04 eV	–0.67 eV	–0.82 eV
B-doped carbon	–1.18 eV	–2.79 eV	–1.15 eV

the strong interaction between B-doped carbon and polysulfides, static adsorption tests were carried out by adding the same amount of the host materials (50 mg) into Li_2S_6 solution (prepared by dissolving Li_2S and S in a molar ratio of 1:5 in the electrolyte). As shown in Fig. S7 in the ESM, although the brownish red Li_2S_6 solution turned colorless after mixing with BPCS-800 and BPCS-800-G for 3 h, mixing with PSC showed almost no change, suggesting that B doping results in strong affinity towards polysulfide absorption, which is in line with the DFT caculations.

Next, we examined the electrochemical performances of the BPCS-800/S and BPCS-800-G/S composites as cathodes for Li-S batteries. Figure 6(a) shows the initial five CVs of the two composites swept at 0.5 $mV \cdot s^{-1}$ in a cutoff window in the range 1.8–2.8 V. The CVs of both composites exhibited two pairs of redox peaks: Two cathodic peaks stemming from the reduction of sulfur (S_8) to higher-order polysulfides (Li_2S_n, $4 \leq n \leq 8$) at high potential, associated with their further reductions to lower-order sulfides (i.e., Li_2S_2/Li_2S) at lower potential [43, 44], and accordingly, two anodic peaks ascribed to the oxidation of Li_2S_2/Li_2S to polysulfides and then to S_8. The BPCS-800-G/S electrode exhibited a larger, more stable redox peak current than the BPCS-800/S one, demonstrating that the introduction of graphene could lead to low polarization and good electrochemical reaction reversibility. In addition, the distinctive positively shifted cathodic peaks and negatively shifted anodic peaks of the BPCS-800-G/S electrode imply that the BPCS-800-G host showed fast kinetics. Galvanostatic cycling measurements were carried out at 0.2 C (1 C = 1,672 $mA \cdot g^{-1}$). The voltage profiles of each composite (Fig. 6(b)) displayed two typical discharge plateaus at ~ 2.33 and ~ 2.07 V and two charge plateaus between 2.18 and 2.40 V, in agreement with the CVs. Figure 6(c) depicts the cyclic performances of the composites measured at 0.2 C. Evidently, the capacity of the BPCS-800-G/S electrode was consistently higher than that of the BPCS-800/S cathode throughout all the cycles. The initial reversible capacity of the BPCS-800-G/S electrode was 798 $mAh \cdot g^{-1}$, and a reversible capacity of 694 $mAh \cdot g^{-1}$ was sustained after 80 cycles, which is considerably higher than that of the BPCS-800/S composite (551 $mAh \cdot g^{-1}$). The compaction densities were 1.66 and 1.69 $g \cdot cm^{-3}$ for BPCS-800/S BPCS-800-G/S, respectively, measured at 10 tons. The higher compaction density of BPCS-800-G/S supposedly represented higher volumetric energy/power density. Moreover, the BPCS-800-G/S composite also showed superior rate capability. As shown in Fig. 6(d) and Fig. S8 in the ESM, the capacities of the BPCS-800-G/S electrode were 1,174, 711, 617, 563, 500, and 395 $mAh \cdot g^{-1}$ at 0.02, 0.2, 0.5, 1, 2, and 5 C, respectively. On the contrary, the BPCS-800/S electrode delivered much lower capacities under the same conditions, particularly at high current rates, for example, 2 and 5 C, clearly showing that graphene ensured faster electron transfer in the BPCS-800-G/S electrode by virtue of the favorable "plane-to-point" conductive mode instead of the sluggish "point-to-point" mode shown by the BPCS-800/S electrode. Of note, compared to the discharge and charge plateaus of the BPCS-800/S electrode, those of the BPCS-800-G/S one had clearly shifted to higher and lower voltages, respectively, at high current densities (≥ 0.5 C), which also corroborates the good electron transport of BPCS-800-G/S. The dramatically decreased charge transfer resistance of the BPCS-800-G/S electrode was further confirmed by EIS analysis, as shown in Fig. S9 in the ESM. The introduction of graphene, on the other hand, can additionally function as a scaffold forming an interconnected porous structure to further restrict polysulfide diffusion, thus leading to better electrochemical performances. Further long-term cycling of the BPCS-800-G/S electrode exhibited a capacity decay of only 0.05% per cycle over 500 consecutive cycles (Fig. 6(e)), demonstrating effective prevention of polysulfide dissolution into the electrolyte. Such exceptional performance is superior or comparable to that of the previously reported heteroatom-doped carbon and carbon-based composite hosts prepared with similar sulfur loadings [34, 45–53], as summarized in Table 2.

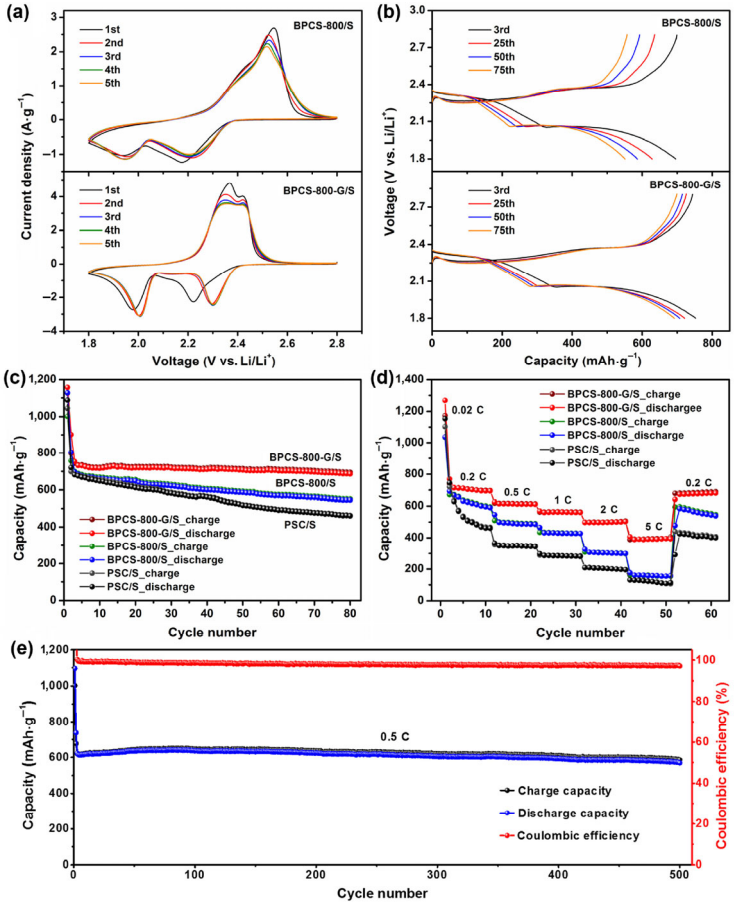

Figure 6 (a) First five CV curves of BPCS-800/S and BPCS-800-G/S composites swept at 0.5 $mV \cdot s^{-1}$. (b) Galvanostatic charge–discharge voltage profiles of BPCS-800/S and BPCS-800-G/S composites measured at 0.2 C. (c) Cycling performances (current rate = 0.2 C) and (d) rate capabilities of BPCS-800/S and BPCS-800-G/S composites compared with those of PSC/S electrode. (e) Long-term cycling stability of BPCS-800-G/S electrode measured at 0.5 C. Cells were cycled at programmed current rates after activation at 0.02 C for initial cycle.

Table 2 Electrochemical performance of BPCS-800-G compared with those of recently reported host materials for Li-S batteries

Sample	Sulfur content	Initial capacity ($mAh \cdot g^{-1}$)	Retention	Rate performance ($mAh \cdot g^{-1}$)	Sulfur loading	Ref.
B-doped porous carbon	67.4 wt.%	~ 790 at 0.1 C	~ 91% after 100 cycles	~ 500 at 0.5 C	~ 1.5 $mg \cdot cm^{-2}$	[46]
N-doped porous carbon/CNT hybrids	62.5 wt.%	~ 800 at 0.5 C	~ 84% after 200 cycles	~ 400 at 2 C	~ 1.5 $mg \cdot cm^{-2}$	[45]
N-doped carbon	60 wt.%	~ 1,120 at 0.48 C	~ 45% after 400 cycles	~ 390 at 0.96 C	0.8–1.0 $mg \cdot cm^{-2}$	[34]
N,O-codoped hollow carbon nanospheres	66 wt.%	~ 1,100 at 0.2 C	~ 74% after 200 cycles	~ 420 at 2 C	~ 1.4 $mg \cdot cm^{-2}$	[47]
N-doped porous carbon	40 wt.%	~ 1,000 at 0.1 C	~ 80% after 100 cycles	~ 500 at 1 C	~ 0.7 $mg \cdot cm^{-2}$	[48]
Graphene/CNT/cobalt	73 wt.%	~ 760 at 0.5 C	~ 61% after 500 cycles	~ 410 at 2 C	1.3–1.6 $mg \cdot cm^{-2}$	[49]
CNTs/CeO_2	60 wt.%	~ 870 at 0.5 C	~ 58% after 600 cycles	~ 700 at 1 C	1.3–1.6 $mg \cdot cm^{-2}$	[50]
Carbon/$FePO_4$	64 wt.%	~ 950 at 0.5 C	~ 58% after 500 cycles	~ 440 at 2 C	~ 1.4 $mg \cdot cm^{-2}$	[51]
Carbon hollow nanoboxes/MnO_2	68 wt.%	~ 1,040 at 0.6 C	~ 45% after 60 cycles	~ 300 at 0.9 C	0.7–1.0 $mg \cdot cm^{-2}$	[52]
Graphene oxide/MnO_2	52 wt.%	~ 1,160 at 0.36 C	~ 43% after 400 cycles	~ 340 at 3.6 C	~ 0.6 $mg \cdot cm^{-2}$	[53]
B-doped porous carbon spheres/graphene	70 wt.%	~ 740 at 0.5 C	~ 78% after 500 cycles	~ 400 at 5 C	1.0–1.3 $mg \cdot cm^{-2}$	This work

For better comparison, PSC was also prepared as a sulfur host. As expected, the PSC/S composite prepared with the same sulfur loading content exhibited poor electrochemical behaviors (Figs. 6(c) and 6(d)) compared with those of the BPCS-800/S and BPCS-800-G/S composites, indicating that B doping had improved the performances of Li-S batteries, in accordance with the above theoretical results. The extraordinary performance of the BPCS-800-G host emphasizes the importance of the dual physical and chemical confinement in enhancing sulfur utilization and in restraining the polysulfide shuttle. In such a fascinating electrode configuration, the high BET surface area and rich porosity are capable of guaranteeing high sulfur loading while simultaneously buffering the changes in sulfur volume during cycling and trapping soluble polysulfides. Aside from that, good electronic conductivity, which can facilitate charge transfer and simultaneously ensure fast kinetics of redox reactions, is also indispensable. Most importantly, the incorporation of B also contributes to the chemical binding of polysulfides, further suppressing their dissolution.

4 Conclusions

In summary, we have developed a facile method of constructing an advanced host composed of BPCSs and graphene for Li-S batteries. The hybrid structure showed good electronic conductivity and combined the physical adsorption and chemical bonding of polysulfides. As a result, the BPCS-G/S electrode exhibited a high reversible capacity of 1,174 $mAh \cdot g^{-1}$, excellent cycling stability with only 0.05% capacity decay per cycle within 500 cycles, and high rate performance (500 and 396 $mAh \cdot g^{-1}$ at 2 and 5 C, respectively). In addition, the origin of the strong polysulfide chemical absorptivity of B-doped carbon was unveiled by DFT calculations and static adsorption tests. Our work offers a general and cost-effective method of synthesizing superior carbon-based materials from low-cost commercially available precursors and more meaningfully highlights the importance of the dual confinement of polysulfides in boosting the electrochemical performances of Li-S batteries.

Acknowledgements

T. Y. acknowledges the supports by MOE Tier 1 (Nos. RG100/15, RG178/15 and RG22/16). W. H. thanks the supports by the National Basic Research Program of China-Fundamental Studies of Perovskite Solar Cells (No. 2015CB932200), Natural Science Foundation of Jiangsu Province (No. BM2012010), Priority Academic Program Development of Jiangsu Higher Education Institutions (No. YX03001), Ministry of Education of China (No. IRT1148), Synergetic Innovation Center for Organic Electronics and Information Displays, and the National Natural Science Foundation of China (Nos. 61136003 and 51173081). J. W. L. thanks the supports from the National Natural Science Foundation of China (No. 21603104). J. F. Z. thanks the supports from the National Natural Science Foundation of China (No. 21502091), Natural Science Foundation of Jiangsu Province (Nos. BK20130912 and 14KJB430017).

Electronic Supplementary Material: Supplementary material (digital photographs of the potato starch, boronated-PS precursor, and BPCS-800-G/S mixture before and after annealing; schematic representation of the synthesis procedure; SEM and elemental mapping images of the BPCS materials; XRD patterns of the samples; SEM images of the BPCS-800/S composite; polysulfides adsorption study; galvanostatic charge–discharge and EIS analysis of BPCS-800/S and BPCS-800-G/S; elemental analysis and N_2 adsorption–desorption data of the samples) is available in the online version of this article at https://doi.org/10.1007/s12274-018-2036-6.

References

[1] Bruce, P. G.; Freunberger, S. A.; Hardwick, L. J.; Tarascon, J.-M. Li-O_2 and Li-S batteries with high energy storage. *Nat. Mater.* **2012**, *11*, 19–29.

[2] Manthiram, A.; Fu, Y. Z.; Chung, S.-H.; Zu, C. X.; Su, Y.-S. Rechargeable lithium–sulfur batteries. *Chem. Rev.* **2014**, *114*, 11751–11787.

[3] Goodenough, J. B. Energy storage materials: A perspective. *Energy Storage Mater.* **2015**, *1*, 158–161.

[4] Yang, Y.; Zheng, G. Y.; Cui, Y. Nanostructured sulfur cathodes. *Chem. Soc. Rev.* **2013**, *42*, 3018–3032.

[5] Manthiram, A.; Chung, S.-H.; Zu, C. X. Lithium–sulfur

batteries: Progress and prospects. *Adv. Mater.* **2015**, *27*, 1980–2006.

[6] Rosenman, A.; Markevich, E.; Salitra, G.; Aurbach, D.; Garsuch, A.; Chesneau, F. F. Review on Li-sulfur battery systems: An integral perspective. *Adv. Energy Mater.* **2015**, *5*, 1500212.

[7] Xu, R.; Lu, J.; Amine, K. Progress in mechanistic understanding and characterization techniques of Li-S batteries. *Adv. Energy Mater.* **2015**, *5*, 1500408.

[8] Titirici, M.-M.; White, R. J.; Brun, N.; Budarin, V. L.; Su, D. S.; del Monte, F.; Clark, J. H.; MacLachlan, M. J. Sustainable carbon materials. *Chem. Soc. Rev.* **2015**, *44*, 250–290.

[9] Liang, J.; Sun, Z.-H.; Li, F.; Cheng, H.-M. Carbon materials for Li–S batteries: Functional evolution and performance improvement. *Energy Storage Mater.* **2016**, *2*, 76–106.

[10] Wang, J. L.; He, Y.-S.; Yang, J. Sulfur-based composite cathode materials for high-energy rechargeable lithium batteries. *Adv. Mater.* **2015**, *27*, 569–575.

[11] Wang, J. L.; Yang, J.; Xie, J. Y.; Xu, N. X.; Li, Y. Sulfur–carbon nano-composite as cathode for rechargeable lithium battery based on gel electrolyte. *Electrochem. Commun.* **2002**, *4*, 499–502.

[12] Wang, J. L.; Liu, L.; Ling, Z. J.; Yang, J.; Wan, C. R.; Jiang, C. Y. Polymer lithium cells with sulfur composites as cathode materials. *Electrochim. Acta* **2003**, *48*, 1861–1867.

[13] Wang, D.-W.; Zeng, Q. C.; Zhou, G. M.; Yin, L. C.; Li, F.; Cheng, H.-M.; Gentle, I. R.; Lu, G. Q. M. Carbon-sulfur composites for Li-S batteries: Status and prospects. *J. Mater. Chem. A* **2013**, *1*, 9382–9394.

[14] Evers, S.; Nazar, L. F. New approaches for high energy density lithium–sulfur battery cathodes. *Acc. Chem. Res.* **2013**, *46*, 1135–1143.

[15] Zhou, G. M.; Tian, H. Z.; Jin, Y.; Tao, X. Y.; Liu, B. F.; Zhang, R. F.; Seh, Z. W.; Zhuo, D.; Liu, Y. Y.; Sun, J. et al. Catalytic oxidation of Li_2S on the surface of metal sulfides for Li−S batteries. *Proc. Natl. Acad. Sci. USA* **2017**, *114*, 840–845.

[16] Pang, Q.; Tang, J. T.; Huang, H.; Liang, X.; Hart, C.; Tam, K. C.; Nazar, L. F. A nitrogen and sulfur dual-doped carbon derived from polyrhodanine@cellulose for advanced lithium–sulfur batteries. *Adv. Mater.* **2015**, *27*, 6021–6028.

[17] Su, D. W.; Cortie, M.; Wang, G. X. Fabrication of N-doped graphene–carbon nanotube hybrids from Prussian blue for lithium–sulfur batteries. *Adv. Energy Mater.* **2017**, *7*, 1602014.

[18] Zhang, C.; Lv, W.; Zhang, W. G.; Zheng, X. Y.; Wu, M.-B.; Wei, W.; Tao, Y.; Li, Z. J.; Yang, Q.-H. Reduction of graphene oxide by hydrogen sulfide: A promising strategy for pollutant control and as an electrode for Li-S batteries. *Adv. Energy Mater.* **2014**, *4*, 1301565.

[19] Radovic, L. R.; Karra, M.; Skokova, K.; Thrower, P. A. The role of substitutional boron in carbon oxidation. *Carbon* **1998**, *36*, 1841–1854.

[20] Yang, C.-P.; Yin, Y.-X.; Ye, H.; Jiang, K.-C.; Zhang, J.; Guo, Y.-G. Insight into the effect of boron doping on sulfur/carbon cathode in lithium–sulfur batteries. *ACS Appl. Mater. Interfaces* **2014**, *6*, 8789–8795.

[21] Xie, Y.; Meng, Z.; Cai, T. W.; Han, W.-Q. Effect of boron-doping on the graphene aerogel used as cathode for the lithium–sulfur battery. *ACS Appl. Mater. Interfaces* **2015**, *7*, 25202–25210.

[22] Jin, C. B.; Zhang, W. K.; Zhuang, Z. Z.; Wang, J. G.; Huang, H.; Gan, Y. P.; Xia, Y.; Liang, C.; Zhang, J.; Tao, X. Y. Enhanced sulfide chemisorption using boron and oxygen dually doped multi-walled carbon nanotubes for advanced lithium-sulfur batteries. *J. Mater. Chem. A* **2017**, *5*, 632–640.

[23] Wu, F.; Qian, J.; Wu, W. P.; Ye, Y. S.; Sun, Z. G.; Xu, B.; Yang, X. G.; Xu, Y. H.; Zhang, J. T.; Chen, R. J. Boron-doped microporous nano carbon as cathode material for high-performance Li-S batteries. *Nano Res.* **2017**, *10*, 426–436.

[24] Wu, F.; Qian, J.; Chen, R. J.; Ye, Y. S.; Sun, Z. G.; Xing, Y.; Li, L. Light-weight functional layer on a separator as a polysulfide immobilizer to enhance cycling stability for lithium-sulfur batteries. *J. Mater. Chem. A* **2016**, *4*, 17033–17041.

[25] Paraknowitsch, J. P.; Thomas, A. Doping carbons beyond nitrogen: An overview of advanced heteroatom doped carbons with boron, sulphur and phosphorus for energy applications. *Energy Environ. Sci.* **2013**, *6*, 2839–2855.

[26] Kiciński, W.; Szala, M.; Bystrzejewski, M. Sulfur-doped porous carbons: Synthesis and applications. *Carbon* **2014**, *68*, 1–32.

[27] Ai, W.; Luo, Z. M.; Jiang, J.; Zhu, J. H.; Du, Z. Z.; Fan, Z. X.; Xie, L. H.; Zhang, H.; Huang, W.; Yu, T. Nitrogen and sulfur codoped graphene: Multifunctional electrode materials for high-performance Li-ion batteries and oxygen reduction reaction. *Adv. Mater.* **2014**, *26*, 6186–6192.

[28] Frisch, M. J.; Trucks, G. W.; Schlegel, H. B.; Scuseria, G. E.; Robb, M. A.; Cheeseman, J. R.; Scalmani, G.; Barone, V.; Petersson, G. A.; Nakatsuji, H. et al. *Gaussian 09*, Revision A.02; Gaussian, Inc: Wallingford, CT, 2016.

[29] Dogru, M.; Bein, T. On the road towards electroactive covalent organic frameworks. *Chem. Commun.* **2014**, *50*, 5531–5546.

[30] Yang, L. J.; Jiang, S. J.; Zhao, Y.; Zhu, L.; Chen, S.; Wang, X. Z.; Wu, Q.; Ma, J.; Ma, Y. W.; Hu, Z. Boron-doped carbon nanotubes as metal-free electrocatalysts for the oxygen reduction reaction. *Angew. Chem., Int. Ed.* **2011**, *50*, 7132–7135.

[31] Ai, W.; Jiang, J.; Zhu, J. H.; Fan, Z. X.; Wang, Y. L.; Zhang, H.; Huang, W.; Yu, T. Supramolecular polymerization

promoted *in situ* fabrication of nitrogen-doped porous graphene sheets as anode materials for Li-ion batteries. *Adv. Energy Mater.* **2015**, *5*, 1500559.

[32] Qie, L.; Chen, W.-M.; Wang, Z.-H.; Shao, Q.-G.; Li, X.; Yuan, L.-X.; Hu, X.-L.; Zhang, W.-X.; Huang, Y.-H. Nitrogen-doped porous carbon nanofiber webs as anodes for lithium ion batteries with a superhigh capacity and rate capability. *Adv. Mater.* **2012**, *24*, 2047–2050.

[33] Xin, S.; Gu, L.; Zhao, N.-H.; Yin, Y.-X.; Zhou, L.-J.; Guo, Y.-G.; Wan, L.-J. Smaller sulfur molecules promise better lithium–sulfur batteries. *J. Am. Chem. Soc.* **2012**, *134*, 18510–18513.

[34] Zhang, J. H.; Huang, M.; Xi, B. J.; Mi, K.; Yuan, A. H.; Xiong, S. L. Systematic study of effect on enhancing specific capacity and electrochemical behaviors of lithium-sulfur batteries. *Adv. Energy Mater.* **2018**, *8*, 1701330.

[35] Zhang, J.; Yang, C.-P.; Yin, Y.-X.; Wan, L.-J.; Guo, Y.-G. Sulfur encapsulated in graphitic carbon nanocages for high-rate and long-cycle lithium–sulfur batteries. *Adv. Mater.* **2016**, *28*, 9539–9544.

[36] Ai, W.; Zhou, W. W.; Du, Z. Z.; Sun, C. C.; Yang, J.; Chen, Y.; Sun, Z. P.; Feng, S.; Zhao, J. F.; Dong, X. C. et al. Toward high energy organic cathodes for Li-ion batteries: A case study of vat dye/graphene composites. *Adv. Funct. Mater.* **2017**, *27*, 1603603.

[37] Rehman, S.; Gu, X. X.; Khan, K.; Mahmood, N.; Yang, W. L.; Huang, X. X.; Guo, S. J.; Hou, Y. L. 3D vertically aligned and interconnected porous carbon nanosheets as sulfur immobilizers for high performance lithium-sulfur batteries. *Adv. Energy Mater.* **2016**, *6*, 1502518.

[38] Ji, X. L.; Lee, K. T.; Nazar, L. F. A highly ordered nanostructured carbon-sulphur cathode for lithium-sulphur batteries. *Nat. Mater.* **2009**, *8*, 500–506.

[39] Zhao, Y.; Wu, W. L.; Li, J. X.; Xu, Z. C.; Guan, L. H. Encapsulating MWNTs into hollow porous carbon nanotubes: A tube-in-tube carbon nanostructure for high-performance lithium-sulfur batteries. *Adv. Mater.* **2014**, *26*, 5113–5118.

[40] Ai, W.; Zhou, W. W.; Du, Z. Z.; Chen, Y.; Sun, Z. P.; Wu, C.; Zou, C. J.; Li, C. M.; Huang, W.; Yu, T. Nitrogen and phosphorus codoped hierarchically porous carbon as an efficient sulfur host for Li-S batteries. *Energy Storage Mater.* **2017**, *6*, 112–118.

[41] Zheng, G. Y.; Yang, Y.; Cha, J. J.; Hong, S. S.; Cui, Y. Hollow carbon nanofiber-encapsulated sulfur cathodes for high specific capacity rechargeable lithium batteries. *Nano Lett.* **2011**, *11*, 4462–4467.

[42] Ji, L. W.; Rao, M. M.; Aloni, S.; Wang, L.; Cairns, E. J.; Zhang, Y. G. Porous carbon nanofiber-sulfur composite electrodes for lithium/sulfur cells. *Energy Environ. Sci.* **2011**, *4*, 5053–5059.

[43] Jiang, J.; Zhu, J. H.; Ai, W.; Wang, X. L.; Wang, Y. L.; Zou, C. J.; Huang, W.; Yu, T. Encapsulation of sulfur with thin-layered nickel-based hydroxides for long-cyclic lithium-sulfur cells. *Nat. Commun.* **2015**, *6*, 8622.

[44] Ghazi, Z. A.; Zhu, L. Y.; Wang, H.; Naeem, A.; Khattak, A. M.; Liang, B.; Khan, N. A.; Wei, Z. X.; Li, L. S.; Tang, Z. Y. Efficient polysulfide chemisorption in covalent organic frameworks for high-performance lithium-sulfur batteries. *Adv. Energy Mater.* **2016**, *6*, 1601250.

[45] Cai, J. J.; Wu, C.; Yang, S. R.; Zhu, Y.; Shen, P. K.; Zhang, K. L. Templated and catalytic fabrication of N-doped hierarchical porous carbon-carbon nanotube hybrids as host for lithium–sulfur batteries. *ACS Appl. Mater. Interfaces* **2017**, *9*, 33876–33886.

[46] Wang, H.-F.; Fan, C.-Y.; Li, X.-Y.; Wu, X.-L.; Li, H.-H.; Sun, H.-Z.; Xie, H.-M.; Zhang, J.-P.; Tong, C.-Y. Fabrication of boron-doped porous carbon with termite nest shape via natural macromolecule and borax to obtain lithium-sulfur/sodium-ion batteries with improved rate performance. *Electrochim. Acta* **2017**, *244*, 86–95.

[47] Peng, Y. Y.; Zhang, Y. Y.; Huang, J. X.; Wang, Y. H.; Li, H.; Hwang, B. J.; Zhao, J. B. Nitrogen and oxygen dual-doped hollow carbon nanospheres derived from catechol/polyamine as sulfur hosts for advanced lithium sulfur batteries. *Carbon* **2017**, *124*, 23–33.

[48] Ji, S. N.; Imtiaz, S.; Sun, D.; Xin, Y.; Li, Q.; Huang, T. Z.; Zhang, Z. L.; Huang, Y. H. Coralline-like N-doped hierarchically porous carbon derived from enteromorpha as a host matrix for lithium-sulfur battery. *Chem.—Eur. J.* **2017**, *23*, 18208–18215.

[49] Zhang, Z.; Kong, L.-L.; Liu, S.; Li, G.-R.; Gao, X.-P. A high-efficiency sulfur/carbon composite based on 3D graphene nanosheet@carbon nanotube matrix as cathode for lithium–sulfur battery. *Adv. Energy Mater.* **2017**, *7*, 1602543.

[50] Xiao, D. L.; Lu, C. X.; Chen, C. M.; Yuan, S. X. CeO_2-webbed carbon nanotubes as a highly efficient sulfur host for lithium-sulfur batteries. *Energy Storage Mater.* **2018**, *10*, 216–222.

[51] Pang, Y.; Wen, Y. P.; Li, W. Y.; Sun, Y. H.; Zhu, T. C.; Wang, Y. G.; Xia, Y. Y. A sulfur-$FePO_4$-C nanocomposite cathode for stable and anti-self-discharge lithium-sulfur batteries. *J. Mater. Chem. A* **2017**, *5*, 17926–17932.

[52] Rehman, S.; Tang, T. Y.; Ali, Z.; Huang, X. X.; Hou, Y. L. Integrated design of MnO_2@carbon hollow nanoboxes to synergistically encapsulate polysulfides for empowering lithium sulfur batteries. *Small* **2017**, *13*, 1700087.

[53] Huang, X. K.; Shi, K. Y.; Yang, J.; Mao, G.; Chen, J. H. MnO_2-GO double-shelled sulfur (S@MnO_2@GO) as a cathode for Li-S batteries with improved rate capability and cyclic performance. *J. Power Sources* **2017**, *356*, 72–79.